

EMISSION SPECTROSCOPY AND RADIOMETRIC MEASUREMENTS IN THE NASA AMES IHF ARC JET FACILITY

Michael W. Winter⁽¹⁾, George Raiche⁽²⁾, Dinesh K. Prabhu⁽³⁾

⁽¹⁾ University of Kentucky, Department of Mechanical Engineering, 261 Ralph G. Anderson Building, Lexington, KY 40506-0503, USA, e-mail: Michael.Winter@uky.edu, Michael.Winter@nasa.gov

⁽²⁾ NASA Ames Research Center, Moffett Field, CA 94035, USA, E-mail: George.A.Raiche@nasa.gov

⁽³⁾ ERC, Inc., NASA Ames Research Center, Moffett Field, CA 94035, USA, E-mail: Dinesh.K.Prabhu@nasa.gov

ABSTRACT

Plasma diagnostic measurement campaigns in the NASA Ames Interaction Heating Facility (IHF) have been conducted over the last several years with a view towards characterizing the flow in the arc jet facility by providing data necessary for modeling and simulation. Optical emission spectroscopy has been used in the plenum and in the free jet of the nozzle. Radiation incident over a probe surface has also been measured using radiometry. Plenum measurements have shown distinct radial profiles of temperature over a range of operating conditions. For cases where large amounts of cold air are added radially to the main arc-heated stream, the temperature profiles are higher by as much as 1500 K than the profiles assumed in flow simulations. Optical measurements perpendicular to the flow direction in the free jet showed significant contributions to the molecule emission through inverse pre-dissociation, thus allowing determination of atom number densities from molecular emission. This has been preliminarily demonstrated with the N₂ 1st Positive System. Despite the use of older rate coefficients, the resulting atom densities are reasonable and surprisingly close to flow predictions. Radiation (from inside the arc column) incident on the surface of a probe in the free jet has been measured. It is shown that this radiation accounts for less than 3% of the total heat flux to a flat surface. The measured spectra show a strong underlying continuum, which is attributed to bound-free radiation generated in the arc column.

1. INTRODUCTION

The development and qualification of heatshield materials for high-speed atmospheric entries relies heavily on ground testing in high enthalpy plasma facilities such as the arc jets at NASA Ames Research Center (ARC). Key parameters for material testing in these facilities are the local enthalpy of the free stream and the heat flux to a probe surface at the test position. Furthermore, computational fluid dynamics CFD simulation of the flow field in these facilities is used for an interpretation of experimental results. Therefore, it is highly important to understand how well the numerical simulation captures the actual facility plasma flow.

Emission spectroscopy measurements were carried out in the plenum and in the free jet of the 60 MW Interaction Heating Facility (IHF) at NASA Ames Research Center [1-4] which is one of the NASA Ames arc jet facilities used to simulate the aerodynamic heating that occurs on the nose cap, wing leading edges and other areas of the spacecraft requiring thermal protection.

In the plenum region (the starting point for CFD simulations) of the heater, the gas is considered to be in thermal and chemical equilibrium. Optical emission measurements were made in the visible to near infrared region (500-900 nm) using a specially designed heater segment with optical access. This segment allows for optical examination through seven access ports (one center and six off-axis positions) of the arc-heated flow

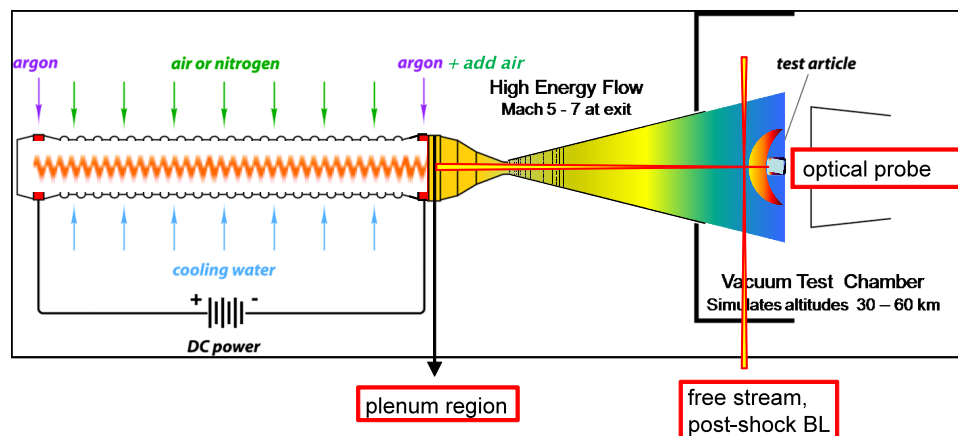


Figure 1. Sketch of the IHF working principle and locations for applied diagnostics.

as it enters the plenum after the downstream electrode, and thus assists in estimating the thermodynamic state of the inflow to the convergent section of the nozzle.

Upon expansion in the diverging section of the nozzle, the chemical composition and vibrational excitation of the gas are most appropriately viewed as frozen. The flow conditions in the free jet determine the consequent heat flux on a probe or sample in the flow. Of particular interest is the chemical composition at the test position since the degree of dissociation significantly affects the total enthalpy of the flow. Emission spectroscopic measurements, with particular focus on atom particle densities, were conducted to determine or infer flow properties. The non-equilibrium aspects of the flow in the free jet were investigated with the inclusion of inverse pre-dissociation processes in the analyses; these processes are not discernable in equilibrium plasmas, but can become dominant under non-equilibrium conditions.

One component of heat flux, which contributes to the total heating of the probe on a sample in the arc-jet flow, is the radiation generated in the arc-heater. Since this radiation heat flux is absorbed to different degrees by metallic surfaces (e.g. calorimeters) and heat shield materials, a biasing of the heat flux measurements might occur if the radiation component is significant. Therefore, the radiation impinging on an optical probe at the test position for material samples was measured with a spectrometer and a radiometer to determine the radiation heat flux during material testing [3, 4]. A description and analysis of the measured data is given for a variety of conditions. Figure 1 shows a sketch of the IHF design and the location of the applied diagnostics.

Data have been acquired at different heater conditions, but in this work, only data for the high condition (6000A arc current, 7300 V arc voltage, main air mass flow of 740 g/sec, chamber pressure of 886 kPa, bulk enthalpy of 21.6 MJ/kg) are presented.

2. THEORY/MODELING

The gains made in modeling of high-temperature thermochemical nonequilibrium flowfields, and advances made in rapid and efficient numerical solvers for such models, have enabled the development of frameworks for analysis of arc-heated flows expanded using a nozzle [5]. The analysis framework makes use of the fact that the geometry of test nozzles is well

known, and that the nozzle-calorimeter combinations are usually fixed. Therefore, there is only an one-time investment in building grids required for numerical simulation; grid generation is usually a long-lead item in the computational process. The computational domain contains the plenum, the convergent-divergent nozzle, and the free jet. Since the nozzles are almost always underexpanded (i.e., $p_{\text{exit}} > p_{\text{test chamber}}$), the free jet is truncated in such a way as to allow imposition of supersonic extrapolation at the boundaries. The calorimeter/test article is considered as an integral part of the computational domain. Such an approach allows for consideration of flow non-uniformities (in either enthalpy and/or mass flux). In order to speed up the analysis process, axial symmetry is assumed. Although the analysis process has been streamlined, there are several uncertainties and unanswered questions regarding the flow, especially the radial distribution of enthalpy (i.e., enthalpy non-uniformity) in the jet.

In the present efforts, a volume grid has been constructed for the 13-inch nozzle of the IHF and free jet without any calorimeter or test article. The axisymmetric version of the CFD code *DPLR* [7] solves the equations governing the temporal development (to steady state) of a flow consisting of 12-species (N_2 , O_2 , NO , NO^+ , N_2^+ , O_2^+ , N , O , N^+ , O^+ , e^- , Ar) in thermochemical nonequilibrium. The facility measured flow rates (of air and argon), and arc column pressure are used to estimate the bulk enthalpy of the arc-heated flow in the plenum section. Using an in-house code, *NOZZLE_THROAT_CONDITIONS*, the radial profiles of enthalpy and mass flux are predicted assuming Gaussian distributions based on nullpoint surveys of the free jet. Further details of the computational process/procedure can be found in Ref. [5].

From the converged solution, profiles of the translational/rotational and vibro-electronic temperatures, and number densities of all the constituent species are extracted at the geometrical positions covered by the optical ports for the plenum measurements, and at a distance of 10 inches from the nozzle exit plane for the free-stream experiments as shown in Figs. 3 and 4.

Fig. 3 illustrates the radial profile of particle densities (in parts/m^3) and temperatures in the plenum (equivalent to the conditions along the centered chord line of sight). Temperatures between 7000K and 8000K are obtained, oxygen (O_2) is almost fully

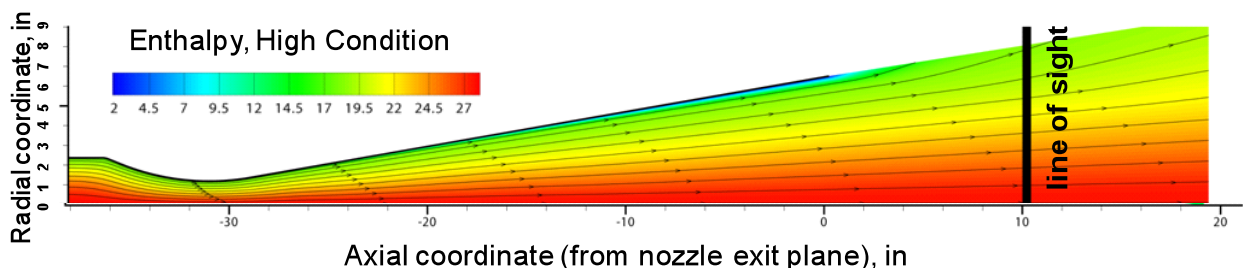


Figure 2. Numerically computed enthalpy distribution in plenum, nozzle and free stream, of the IHF.

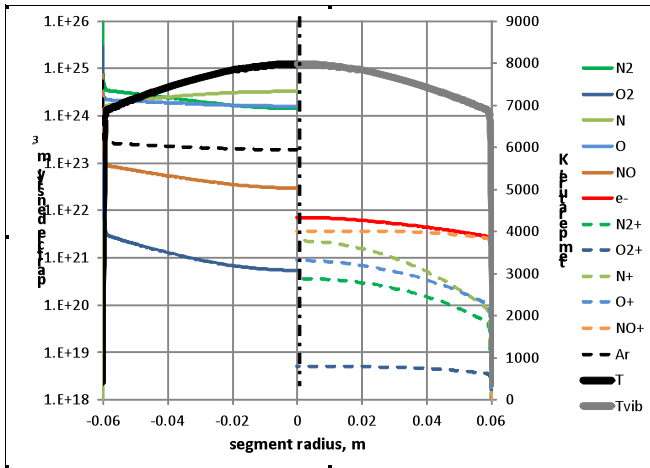


Figure 3. Simulated temperatures and particle densities (neutrals left, ions right) along the center chord in the IHF plenum region.

dissociated over the whole cross section, nitrogen dissociation reaches about 70% at the center, and ionization reaches a maximum of roughly 0.1%, the main ion being NO^+ .

In the free stream, the simulation shows a rather flat profile of translational temperature between 2000 K and 2150 K for radial positions less than 13 cm and drops down rapidly for higher radial positions as illustrated in Fig. 4. In the same region, the vibrational temperature has a more distinct profile with a maximum value of 3200 K, which flattens out near the wall at about 2700 K. Oxygen is found to be almost completely dissociated, while nitrogen dissociation has a distinct profile peaking on axis with a value of roughly 40%. The ionization fraction is low with maximum values on axis of about 0.01 %.

For all IHF positions under consideration, simulated lines of sight are extracted from the computed profiles, and the data are used in the *NEQAIR* 2009 V6.9, which is a line-by-line spectroscopic code with one-dimensional transport of radiative intensity [9]. It computes the emission and absorption of atoms (N, O, H, C, He) and molecules (N_2 , N_2^+ , NO, O_2 , H_2 , CO, C_2 , CN) as well as bound-free and free-free continuum radiation caused by interactions of electrons with neutral and ionized atomic species. Line broadening due to Doppler, Stark, resonance, and collisional mechanisms as well as the natural line width are included as a Voigt function, and an additional Voigt

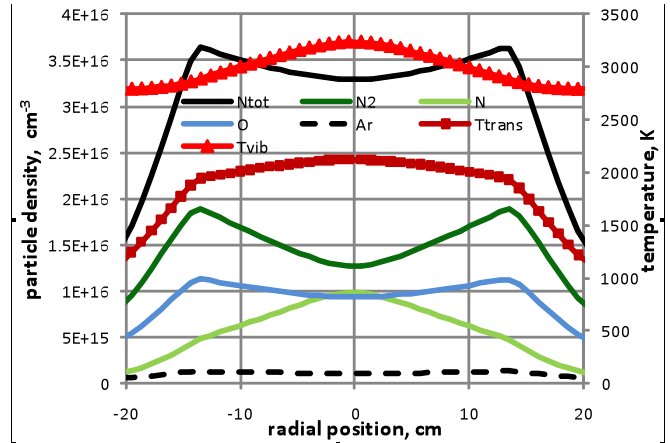


Figure 4. Temperature and particle density profiles along the center chord line of sight at a distance of 10 inches to the nozzle exit, extracted from the *DPLR* simulation.

broadening can be applied to account for instrument broadening. Radiative transport is computed along a line-of-sight as a series of one-dimensional cells – a tangent slab approximation. In absence of an individual electron temperature in the two-temperature model used in *DPLR*, the vibrational temperature is used for electronic excitation.

Principal molecular band systems considered for the free stream condition are the 1st and 2nd positive systems of N_2 , the 1st negative system of N_2^+ , the γ , β , δ , and ϵ systems of NO. High-resolution spectra were computed using *NEQAIR* for these band systems and were convolved with the experimentally determined instrument function to produce synthetic spectra for comparison against the measurements.

3. II. Facility and Optical Set-up

The 60 MW Interaction Heating Facility (IHF), one of several arc jet facilities at NASA Ames Research Center, is used to test and qualify spacecraft thermal protection materials in “flight-like” aerothermal environments. The IHF heater uses a constricted arc design with an upstream anode and a downstream cathode, both consisting of 8 electrode disks. The working gases are injected throughout the arc column established between the anode and the cathode, and are heated to very high temperatures. The magnitude of the temperatures, and hence the flow energy, depends on

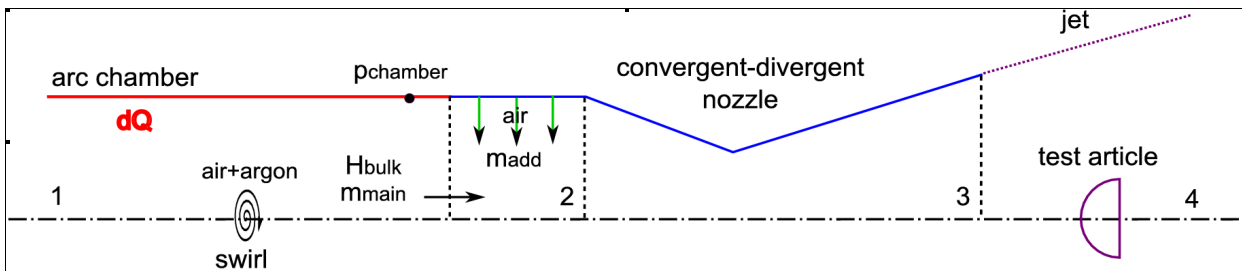


Figure 5. Sketch of the IHF working principle.

the input current, voltage, and flow rates. Following the cathode, there are 4 disks/segments through which additional room temperature air (in the following referred to as “add-air”) can be injected to tailor the enthalpy to the desired test value. This set of 4 segments is referred to as the “plenum” in the present work. The working gas, of appropriate enthalpy, is then expanded through a convergent-divergent nozzle, and the test article is placed in the free jet. Figure 5 shows a sketch of the IHF design.

The operating conditions of the facility are mainly characterized by arc current and voltage, and the different mass flows (main air, add air and argon) yield a chamber pressure and bulk enthalpy derived from the balance of input power and cooling losses. Several operating conditions have been covered through optical measurements. For the present work, however, only the condition at high power with minimum add-air (high enthalpy) is considered.

3.1 Optical Setup for Plenum Diagnostics

Since the plenum region is not amenable to intrusive measurement/diagnostic techniques, optical methods have to be used. Therefore, between the add-air disks and the convergent part of the nozzle, a spacer disk with optical access was inserted. Figure 6 illustrates the geometric configuration of this disk with optical access. The disk has 7 access ports at different cross sections. To feed the optical signals out of this closed environment, optical fibers are used. Due to the geometry of the facility, the minimal fiber lengths were 3.5 m and 4.5 m for the west and east side access points, respectively. The 7 ports are used for the reconstruction of radial distributions based on measured emission signatures.

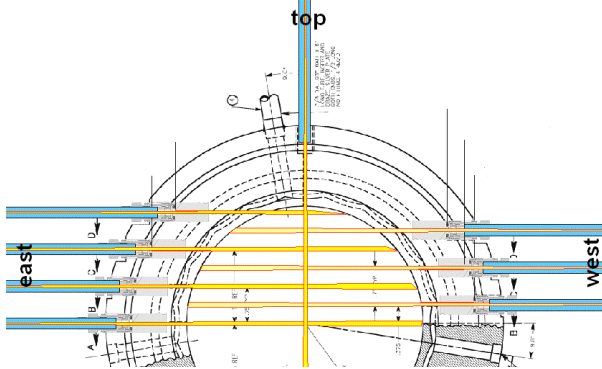


Figure 6. Illustration of the geometrical configuration of the optical plenum disk.

An Acton SP300i and an intensified Princeton PI-max camera were used for detection. To feed all fibers simultaneously into the spectrometer, a customized fiber coupler, which combines the seven single fiber

legs into a linear array, was used. Each leg consisted of a fiber bundle of seven individual fibers. The single channels were then imaged on to different vertical positions on the CCD array of the intensified camera. Figure 7 shows the resulting image of the fiber configuration on the CCD for a typical spectrum. Out of the single fibers for each channel, only the inner 5 were integrated to the final signal to avoid charge bleed artifacts between the different channels.

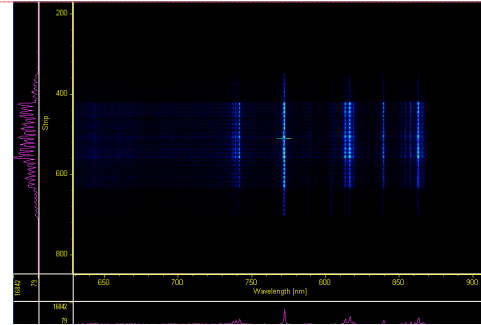


Figure 7. Raw data of a typical plasma showing the coupling of the fibers to spectrometer and CCD.

The measurements were calibrated to absolute spectral radiance units using a calibrated integrating sphere. For the calibration, a spare optical segment was cut in two halves to be able to place the calibration lamp on the axis. Initial ray tracing analysis of the optical path indicated that the sensitivity along the line of sight should be constant. However, measurements with the calibration lamp at different positions on the line of sight showed a small variation of the measured signal on the order of 2%, which was neglected. Recent measurements during the optical probe campaign with a remodeled optical segment [4] indicate that the spatial sensitivity of the calibration segment might show differences to the actual plenum segments, leading to biasing factors for the different channels. This effect is still under investigation and might yield modification of the existing data towards higher measured intensities.

3.2 Optical Setup for Free Stream Diagnostics

Reliably calibrated data were acquired at a position 10 inches (254 mm) downstream of the nozzle exit covering a maximal wavelength range of 200 nm to 1000 nm with different spectrometers (Ocean Optics S2000, Acton SP300i + PImax CCD) with full widths at half maximum (FWHM) of 4.5nm and 1.1nm, respectively. The plasma on the generator axis at a distance of 2.1 m to the focusing spherical mirror ($f=305$ mm) was imaged on a bifurcated optical fiber which allowed for simultaneous measurements of two channels. The f number of the fiber (numerical aperture $n_A=0.22$) was matched using an aperture between mirror and fiber. Radial profiles were obtained by inclining the focusing set-up, thus measuring tilted

lines of sight through the plasma beam characterized by the radial co-ordinate in the center of the line of sight. A total of six lines of sight contained significant signal, measured at offsets of 3mm, 59 mm, 92 mm, 117 mm, 144 mm and 168 mm. At higher offsets, the measured signal contained mainly noise.

The measurements were calibrated to absolute intensities using an integrating sphere and a Deuterium lamp, which were placed on the center axis of the facility.

3.2 Optical Probe

The probe design is based on a water-cooled probe body that carries an optical plug with a sapphire window to seal the optical path against the post shock plasma and a mechanical connection for an optical fiber. On the arc-jet side, the limiting aperture is the nozzle throat, which defines the necessary field of view. On the probe side, the front mask is the limiting aperture stop. The optical path is limited through aperture stops only, without focusing elements. Thus, each point in the field of view sees, in good approximation, the same receiving surface (the fiber aperture or the radiometer pinhole) that corresponds to very similar solid angles in which radiation is emitted. The sensitivity is almost constant across the field of view [3]. At a probe position of 3 inches from the nozzle exit of the IHF equipped with the 6" nozzle, the half-angle of the necessary field of view becomes 4.4° which is also the maximum angle under which radiation has to be fed into the fiber or to the thermopile sensor.

The spectrometer (Avantes AvaSpec-3648-USB2-UA, nominal wavelength range 180-1100nm) was located outside the arc-jet test box and the optical signals were fed to the spectrometer by optical fibers. The front plug can be inserted and taken out while the probe is mounted and aligned. Therefore, different entrance apertures can be used without changing the alignment. The radiometer design contains a Dexter Research ST-120 temperature compensated thermopile as sensing element and in house custom sensor electronics inside the sting arm. Temperature compensation is achieved through a second thermopile sensor which is shielded from the radiation and therefore experiences environmental changes (i.e. usually temperature changes of the whole sensor) the same way as the radiation sensing thermopile and can be used to compensate for these changes. An extrapolation of radiation fluxes from previous spectrometer measurements lead to anticipated radiation levels of up to 70 W/cm^2 . The sensor, however, had a destruction limit of 100 mW/cm^2 . Therefore, a $50\mu\text{m}$ pinhole was added to the optical path, limiting the incident total radiation. The sensing area ($1.2 \times 1.2\text{mm}^2$) itself was placed at a defined distance to this pinhole. The optical path was chosen to blur the radiation flux on the

pinhole to a value acceptable for the sensor (i.e. by a factor of about 500 in the given configuration).

For the spectroscopic measurements, the optical probe was swept through the free jet (Fig. 2) with a defined sweep velocity. During the sweep time the spectrometer continuously acquired data and stored them in the local (on-board) memory. Maximum data acquisition speeds are on the order of 250 Hz with minimum acquisition times of $1.1\mu\text{s}$ for each individual spectrum. The data acquisition of the spectrometer was triggered by a 5 V TTL (Transistor-Transistor Logic) pulse once the probe was set into motion. Both trigger and position readings of the sting arm were stored in the facility data acquisition system to enable synchronization with the spectra stored in the internal memory of the spectrometer. Figure 8 illustrates the measurement strategy showing three probe positions during the sweep; firstly with the probe outside the flow, then looking at the nozzle wall with a shock already building up, and finally at the center line measuring the sum of plenum and post-shock emission. However, the results showed that the contribution of the post shock radiation can be neglected in the given probe configuration.

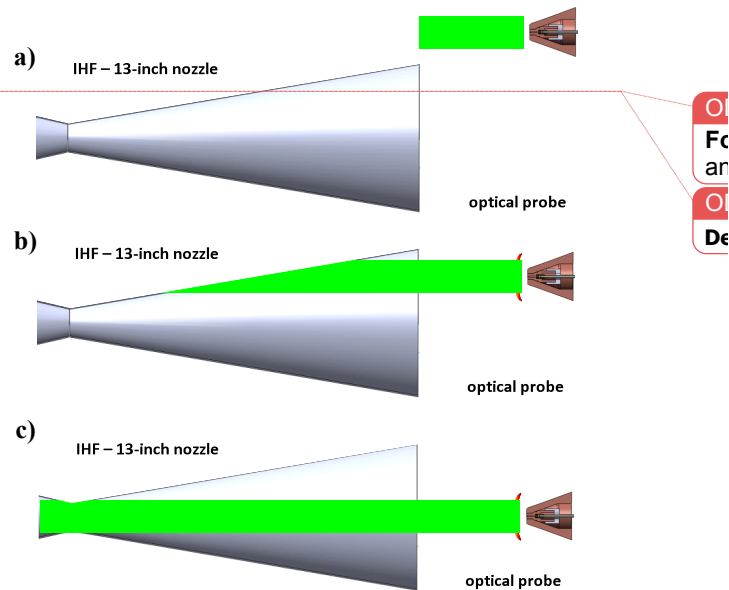


Figure 8. Measurement strategy during Optical Probe sweep through the plasma flow of the IHF arc-jet. a) Optical probe outside the plasma flow, b) probe “seeing” the cold wall, and c) at the centre line.

The useful wavelength range of the combination of optical fibers, neutral density filters, and spectrometer was 250-950nm with a full width at half maximum (FWHM) of about 1.3nm. Acquisition times during arc-jet testing varied between $10\mu\text{s}$ and 4ms.

In addition to the spectrometer probe, a radiometer was placed in a second cone on a different sting arm to provide total radiation measurements during the same arc-jet run. Spectrometer and radiometer data were

calibrated through measurements of integrating spheres (and a Deuterium lamp for the spectrometer). For the final calibration of the radiometer, the custom made electronic board was replaced by a Stanford Research Systems low noise amplifier. The transfer function of the electronic circuit board used during testing was measured separately.

4. Experimental Results

Different conditions were investigated with each method. For the plenum diagnostics, data for a high enthalpy condition with no added air and one low enthalpy condition with a substantial amount of add-air are presented since the findings for both cases are significantly different. For free stream diagnostics and the radiometric and spectroscopic data looking from the probe position into the heater, only data for the high enthalpy condition is shown here.

Plenum diagnostics

As mentioned above, experimental spectra calibrated through the calibration segment and with the calibration lamp placed inside the original heater segment yielded a significant difference in measured signal strength, with the directly calibrated values being higher by a factor of about two. Due to geometrical constraints, direct calibration could only be applied to the center port. Additional sensitivity measurements are in preparation for all ports. Until these data are available, the conclusions are still considered preliminary. However, with these corrections applied to the center port measurements, the radial profiles come closer to anticipated shapes, showing a maximum at the center instead of a local minimum and a reasonably smooth profile towards the wall. Therefore, the results shown here include the directly calibrated center port measurements and the off-axis positions calibrated through the measurements with the calibration segment.

Due to the high temperatures in the plenum region, substantial dissociation is seen and the major emission comes from atomic lines of oxygen and nitrogen. A comparison between simulated and measured spectra in the wavelength region between 650nm and 915nm is shown in Fig. 8 for the center line port. The spectra are qualitatively very similar but the measured data are higher by a factor of about two.

Since the atomic lines are the major radiators, the intensities of the oxygen lines at 777 nm and 845 nm and the nitrogen lines at 745 nm and around 820 nm were spectrally integrated (in the following this integral is called line intensity) for an analysis of the radial distribution. Using the integrated intensities rather than the peaks accounts for possible differences of the line shape in experiment and simulation.

Trapezoids defined by the integration limits were used to account for underlying continuum and molecule emission in the experimental data. Separate simulations with only oxygen or nitrogen as radiating species were used to determine the theoretical line emission. The resulting radial distributions are used to compare simulation and experiment.

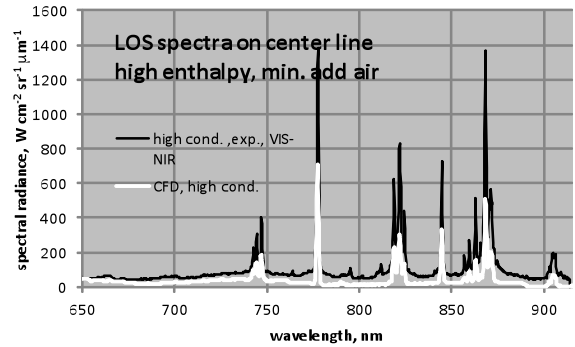


Figure 8. Simulated and measured emission spectra between 650 nm and 900 nm on the center line at the high enthalpy condition.

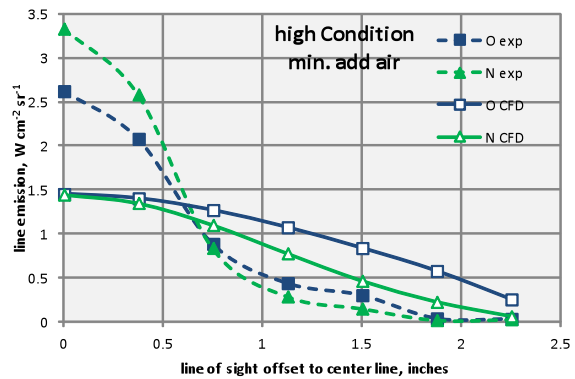


Figure 9. Predicted and measured radial profiles of O and N line intensities at the high enthalpy condition vs. line of sight offset from center line.

Since the plasma is considered to be in equilibrium at these high pressures (up to 8 atm), the atom emission can be computed as a function of temperature only using Boltzmann distributions. However, the atom concentrations will also be a function of the equilibrium temperature. Oxygen stays almost fully dissociated in the temperature range of concern. Therefore, as a first order approach, the difference between measured and predicted radiation from atomic oxygen is interpreted as an upper limit for the necessary modification of equilibrium temperature to match the experimental data.

For the high condition, the atom emission in comparison to the simulation is higher close to the center of the segment. However, a more narrow profile with a stronger decrease in emission can be observed towards the wall, as shown in Fig. 9. Consequently, this yields slightly higher equilibrium temperatures at

the center by about 300K but a stronger temperature decrease towards the wall, yielding measurement based equilibrium temperatures lower by up to 700K close to the wall (Fig. 10).

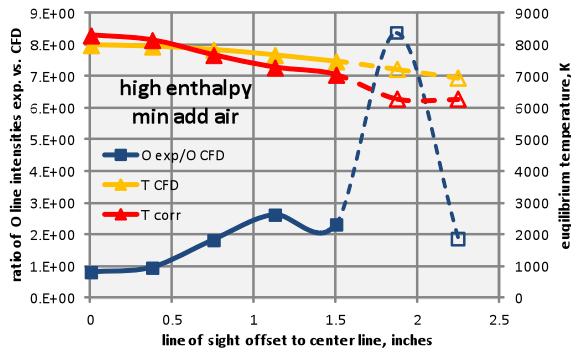


Figure 10. Oxygen line intensity ratio between CFD and experiment, CFD temperature, and measurement based temperature vs. line of sight offset from center line at the high enthalpy condition.

For the condition with significant add-air, spectra, atom line intensities, and corrected temperatures are shown in Figs. 11-13. The experimental spectra are significantly higher than the simulation based on CFD. Even from the qualitative comparison, a higher temperature can be seen in the experiment since the emission of atomic nitrogen is clearly seen in the experimental data while the nitrogen lines do not even show up in the simulation data if viewed on linear scale.

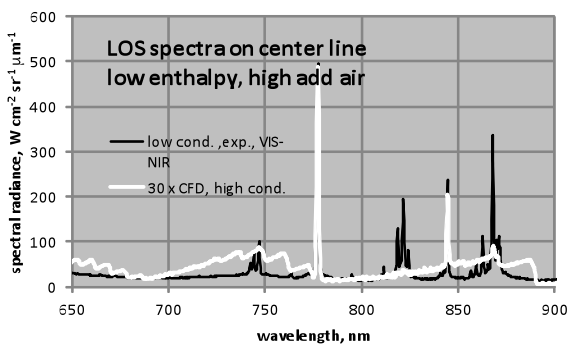


Figure 11. Simulated and measured emission spectra between 650 nm and 900 nm on the center line at the low enthalpy condition.

An under prediction of the oxygen emission by a factor of 50 is observed on the center line. For nitrogen, this factor increases to ~1000. If the same approach of interpreting these factors as a necessary modification of equilibrium temperature is applied, the CFD temperature needs to be higher by up to ~1500K throughout the whole profile.

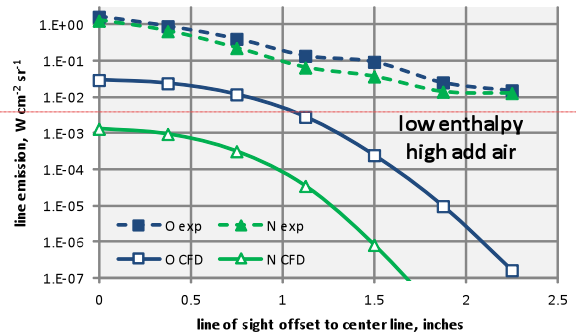


Figure 12. Predicted and measured radial profiles of O and N line intensities at the low enthalpy condition vs. line of sight offset from center line.

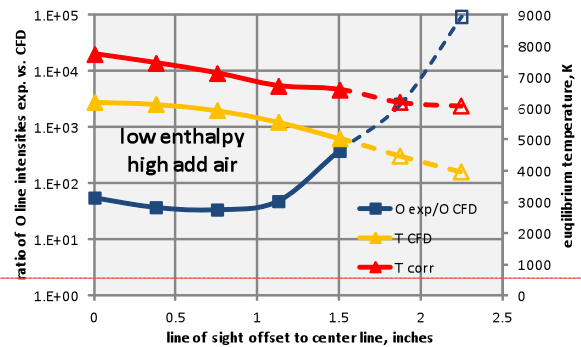


Figure 13. Oxygen line intensity ratio between CFD and experiment, CFD temperature, and measurement based temperature vs. line of sight offset from center line at the low enthalpy condition.

For a further interpretation of these data, a parameterized variation of equilibrium profiles for each condition is being computed to be used as input for *NEQAIR* computation. Through an optimization of the underlying temperature profile, a best matching spectral simulation is anticipated to be found, which should yield an enthalpy profile to match the measurements. If a characteristic pattern can be found once this process is performed for a number of conditions, this data might serve as experimental input to the starting condition for CFD computation of the heater flow.

Free Stream Diagnostics

The data presented here were taken with different set-ups in different resolutions over a period of about 2 years, with independent calibrations. The spectra data obtained with the different set-ups are in excellent qualitative and quantitative agreement, which underlines the stability of the condition.

The spectra were dominated by the emission of different NO systems in the UV and by the emission of the 1st Positive system of N₂ (B-A transition) in the visible (VIS) and near infrared (NIR). No significant atom emission could be detected.

In a first approach, simulated spectra were generated by using the *DPLR* solution along the lines of sight as input for *NEQAIR*. However, the measured data differ substantially from the prediction, both in intensity and shape. Therefore, the simulations were repeated for each radiating species separately to be able to scale the different spectral components individually.

In the UV region, the center line spectra could not be rebuilt with the CFD vibrational temperature used as the electronic excitation temperature -- overpopulation factors of about 6 orders of magnitude were required to match experimental and simulated NO radiation as demonstrated in Fig. 14.

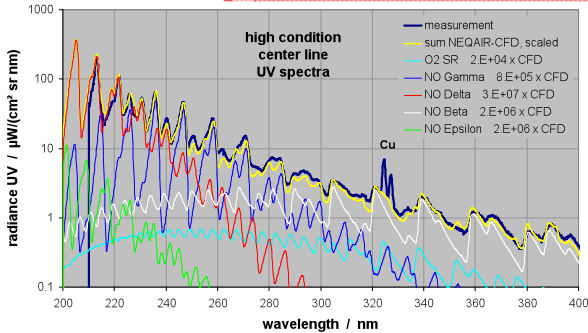


Figure 14: Measured UV spectrum at high condition and scaled CFD simulation.

To account for this overpopulation, excitation temperatures on the order of 9000 K would be needed instead of the 3200 K temperature taken from *CFD*. Similar temperature values have already been reported in earlier investigations of arc-jet flows [11, 13] and might be attributed to an insufficient representation of the non-equilibrium environment by the two-temperature model used in *DPLR*. However, in comparison to the other NO systems, an overpopulation of the NO C state remains even if a separate electronic excitation temperature is adopted. This indicates the presence of inverse pre-dissociation processes as successfully introduced by Seong et al. [11] for the interpretation of similar data obtained in the NASA Ames Aero Heating Facility (AHF) [13]. Future analysis of the spectra will focus on this topic.

In the VIS/NIR region between 500nm and 900nm, the spectrum is dominated by emission from the N_2 1st Positive system as shown in Fig. 15 a). The simulation based on Boltzmann populations for the rotational and vibrational excitation does not even qualitatively fit the measured data as seen in the same figure. However, if the theoretical spectra are computed separately for each upper vibrational quantum number to all allowed lower levels and if these spectra are appropriately scaled and summed, the spectrum below 800nm can be reasonably well matched as shown in Figure 15 b).

Best agreement was achieved for wavelength regions which are dominated by high vibrational quantum numbers (i.e. between 520nm and 600nm). The highest

disagreement (and therefore the highest uncertainty of the scaling factors) is seen in wavelength regions dominated by the emission due to low vibrational quantum numbers. The emission from $v'=0$ was outside the measured wavelength range.

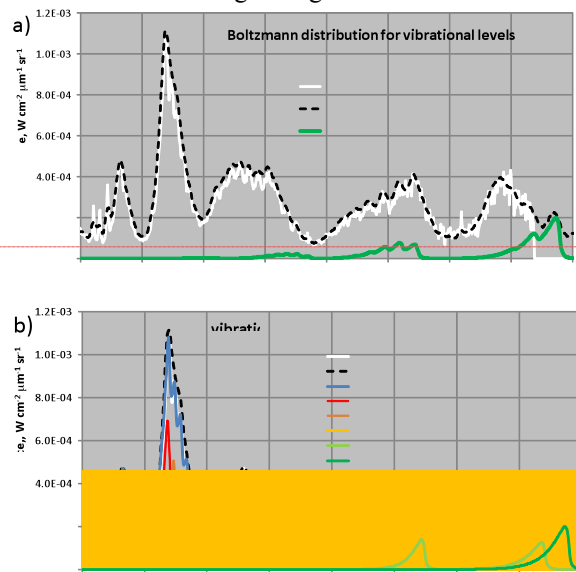


Figure 15: Measured VIS/NIR centerline spectra at high condition and scaled CFD simulation with modified N_2 B state vibrational populations for selected levels.

To analyze these spectra, the population of each upper vibrational state was extracted from *NEQAIR*. By multiplying the above scaling factors with these upper state densities, a measured upper state population density for each vibrational quantum number is obtained. These numbers are independent of temperature or equilibrium assumptions which were used to generate the original spectrum.

In the *NEQAIR* simulation based on the *CFD* solution, the upper vibrational levels are populated through a Boltzmann distribution. The population densities are decreasing with vibrational quantum number in an exponential manner as shown in Fig. 16 (a). Here, the population densities are integrated along the simulated line of sight, therefore given as a column density of units cm^{-2} . The population of high vibrational levels is very low -- almost 100% of the population of the electronic state can be found at vibrational quantum numbers lower than $v_u = 7$.

The measured vibrational population, on the other hand, decreases from high values at low vibrational quantum numbers up to $v_u = 7$ but starts increasing again with maximum values at $v_u = 13$ as shown in Fig. 16 (b). Almost half of the measured population density of the electronic state (excluding $v_u = 0, 1$) can be found in levels with $v_u > 7$. As discussed earlier, the measured data are considered less reliable for lower

vibrational quantum numbers, therefore the curves are plotted with dashed lines for $v_u < 7$.

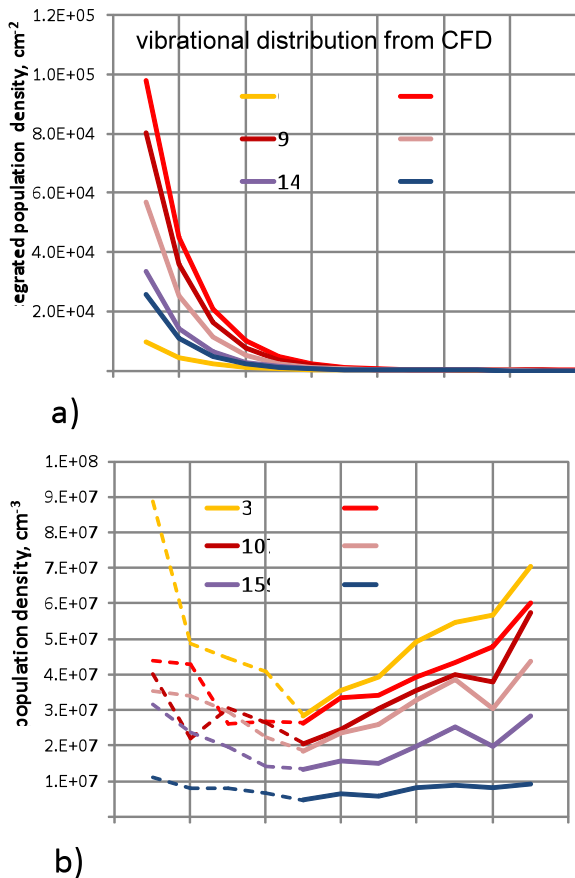


Figure 16: Population densities of different vibrational levels of the N_2 B state based on a) CFD simulation and Boltzmann distribution and b) Abel inverted measurements.

The emission of nitrogen molecules due to excited state chemistry also appears in afterglows such as the Lewis-Rayleigh afterglow [15]. One major process is the inverse pre-dissociation of ground state atoms $[N(^4S)]$ into excited molecular states of nitrogen. Due to the quantum mechanical selection rules, the ground state atoms can only form the $X^1\Sigma_g^+$, $A^3\Sigma_u^+$, $A'^5\Sigma_g^+$, and $7^5\Sigma_u^+$ states, of which the latter one is repulsive [18]. These states (in particular $N_2 A'^5\Sigma_g^+$) then, through collisions and/or level crossing processes, may populate preferred vibrational levels of other states such as $N_2 B^3\Pi_g$ and $N_2 B^3\Sigma_u^+$, which are the upper states of dominant radiative transitions such as the N_2 1st Pos. system ($N_2 B^3\Pi_g \rightarrow N_2 A^3\Sigma_u^+$) or the N_2 afterglow system ($N_2 B^3\Sigma_u^+ \rightarrow N_2 B^3\Pi_g$). Pre-dissociation and level crossing into the $N_2 B^3\Pi_g$ state is known to preferably populate $v_u=13$ [11]. For the population of lower vibrational levels, different explanations are given e.g. by intrastate vibrational relaxation or collisional

population from other electronically excited states (e.g. collisional population of $N_2 B^3\Pi_g$, $v_u=0-2$ from $N_2 A^3\Sigma_u^+$, $v_u=7-9$), or three body recombination of atomic nitrogen [15].

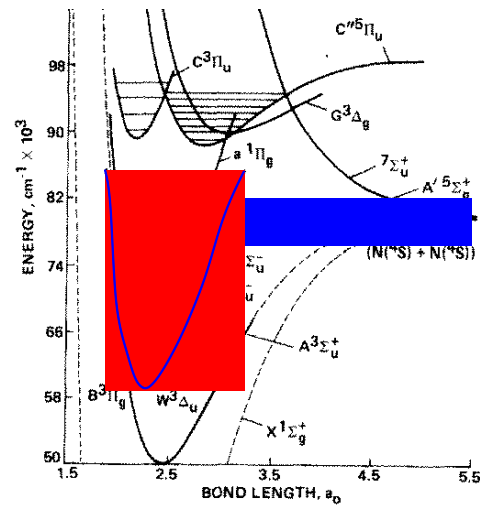


Figure 17: Potential crossing between the $N_2 A'^5\Sigma_g^+$ and $N_2 B^3\Pi_g$ states.

The level crossing processes have been investigated by Partridge et al. [18] who showed that a level crossing from the $N_2 A'^5\Sigma_g^+$ state to the $N_2 B^3\Pi_g$ state can only occur into vibrational levels with $v_u > 10$, and higher vibrational levels showing a larger potential overlap, thus giving higher crossing rates.

In the experimental data, no significant contributions of vibrational levels higher than $v_u = 13$ could be found. This is consistent with the measurements of Laux et al. [15] and Ung [17] who also suggested that the principle mechanisms for the population of $v_u > 13$ are substantially different from those populating $v_u = 13$. These correlations are interpreted as a clear indication for the inverse pre-dissociation through the $N_2 A'^5\Sigma_g^+$ state being a dominant process for the molecular radiation at the measured conditions. To further interpret these results, the sum of all populating and depopulating processes for the N_2 B state are to be investigated:

- Thermal/vibrational excitation through electron collisions (both populating and depopulating) which requires knowledge of T_{el} , T_{trans} , T_{vib} , n_{el} , n_{N_2}
- Radiative depopulation to the N_2 A state (N_2 1st Pos. System), and radiative cascade population from the N_2 C state (2nd Pos. System).
- Level crossing processes to other excited states
- Quenching due to heavy particle collisions

The following assumptions are employed:

- Thermal/vibrational excitation of the high vibrational levels is negligible, meaning that knowledge of T_{el} or

T_{vib} is not necessarily required if the analysis is restricted to these levels.

- The major radiative processes can be covered through measurements of N_2 1st and 2nd Pos. systems.
- Vibrational relaxation can be covered by integrating over the high vibrational levels or/and extrapolation of the measured levels to the lower ones through an appropriate fit function without employing explicit rates.
- The upper and lower bound for quenching can be determined under assumptions of no quenching and full quenching (i.e. every collision depopulates the excited state).
- Due to the large difference in population densities between the N_2 B state and the N ground state, inverse pre-dissociation will dominate and pre-dissociation can be neglected.

For a first order approach, this leaves as unknowns the rates of level crossing processes and the heavy particle quenching with the assumption of no quenching as a lower bound. If the rate coefficients for the inverse pre-dissociation processes are known, a lower bound for the nitrogen atom particle densities can be derived from balancing the measured N_2 B excited state populations and the atom ground state densities with the inverse pre-dissociation coefficient. Theoretical and experimental investigations of the afterglow describe the pre-dissociation and its inverse. An integral rate coefficient for the inverse pre-dissociation of nitrogen ground state atoms into the upper vibrational state $v_u=12$ of the N_2 B state was for example given by Benson [13] in the form:

$$[N_2(B^{(12)})*] = K_{B*} [N]^2$$

with $K_{B*} = 10^{-3.6}$ litre/mole = 4.17×10^{-25} cm³

As a preliminary consistency check of the excited state populations determined in former investigations [2], the Abel-inverted upper state densities of the N_2 B state between vibrational quantum numbers of $v_u=8$ and $v_u=13$ shown in Fig. 16, were summed, and the corresponding upper bound ground state density of nitrogen atoms was calculated. This implies the assumption that the major population happens through $v_u=12$, and the resulting upper state density is distributed to the other levels through vibrational relaxation. As a lower bound, the same procedure was repeated for the upper state density of $v_u=12$ only under the assumption that no significant depopulation through vibrational relaxation occurs. The results are compared to the nitrogen particle density taken from the CFD solution. The theoretically highest possible nitrogen particle density would be given if all nitrogen was dissociated, therefore this case was computed as well. The results are shown in Fig. 18.

Taking into account the very crude way of computing these values (i.e. neglecting all other population and depopulation processes for the N_2 B state and the fact that Benson's reaction coefficient is given for a temperature of 300K) the results agree very reasonably with the CFD solution. In fact, the solution using the upper state density of $v_u=12$ only reproduces the CFD values rather well. Similar processes can be formulated for NO [11] giving access to the product of ($[N]$ $[O]$). Currently, rate coefficients for the excited state chemistry of N_2 are being determined from ab-initio computations at NASA Ames which are anticipated to yield a more accurate analysis of these data.

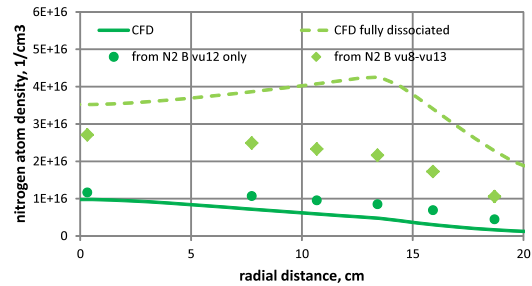


Figure 18: Atom densities computed from N_2 B upper state densities in comparison to CFD data.

Incident Radiation on an Optical Probe

Data with both 6-inch and 13-inch nozzles were taken at positions of 3 and 10 inches to the nozzle exit, respectively. Repeated measurements during different sweeps at the same condition gave fairly consistent results. The spectra are dominated by a strong continuum overlaid by bound-bound radiation from atomic nitrogen and oxygen and from molecular systems from N_2 and N_2^+ . If an arbitrary continuum is fitted to the spectra, the bound-bound radiation can be separated from the measured spectra by subtracting this continuum. The spectral distribution of incident spectral irradiance (or spectral radiative heat flux) between 250 and 950nm on the IHF center-line and the resulting continuum and bound-bound spectra for the high enthalpy condition (MSL-8) with the 6-inch nozzle are shown in Fig. 19.

The main bound-bound radiation at wavelengths above 600nm comes from oxygen and nitrogen atom lines. Below 500nm, the molecular bands from N_2 and N_2^+ in the near ultraviolet are strong emitters. NO radiation is expected to dominate below 250nm. The continuum radiation increases with lower wavelengths and peaks slightly below 350 nm. At the MSL-8 condition, 80% of the measured radiation comes from continuum emission. Although *NEQAIR* [9] simulations based on solutions of the flow field starting in the plenum of the arc-heater all the way downstream to the probe position are available, it has been shown in the analysis of the results with the 13-inch nozzle that the main radiation

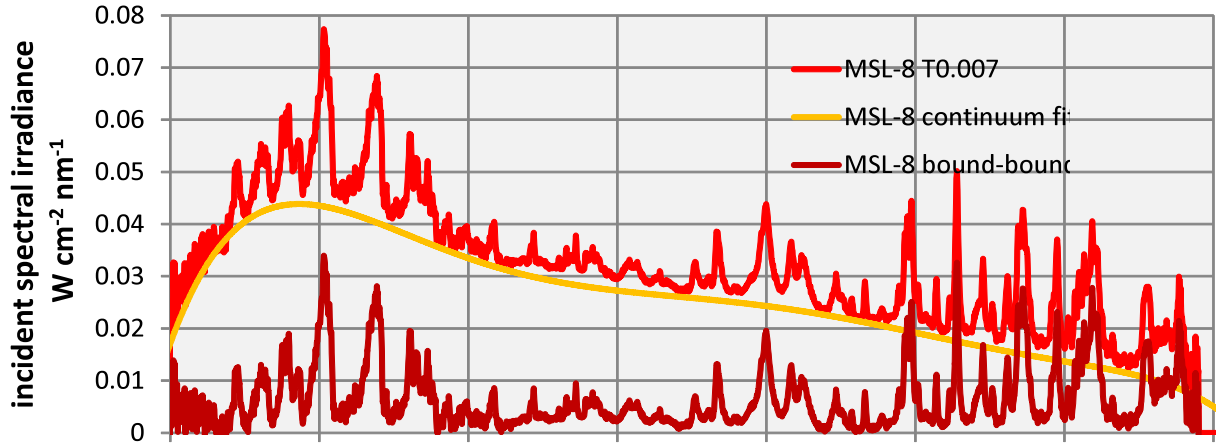


Figure 19. Measured spectral irradiance, continuum fit to these spectra, and resulting bound-bound spectra at the MSL-8 condition.

seen by the optical probe is generated upstream of the simulation regime [3]. In particular, the experimentally observed continuum radiation is not present in the simulation.

As expected, the measured spectral irradiance at the 6-inch nozzle location shows a significant increase in comparison to the measured data at the 13-inch nozzle location. The spectra are qualitatively similar but the ratios for bound-bound and continuum radiation are different. For the MSL-8 condition, the bound-bound radiation increased by a factor of 5.25 while the continuum only increased by a factor of 2.45.

Since the internal flow field inside the arc heater does not depend on the choice of nozzle, the incident irradiance (or radiation heat flux) at the probe position only depends on geometric view factors (assuming the contribution of the post-shock system in front of the probe to be negligible). The test location for the 6-inch nozzle is at a distance of 3 inches to the nozzle exit. The distances to the nozzle throat are 11.3 inches and 31.2 inches for the 6-inch nozzle and the 13-inch nozzle, respectively. With both nozzles, the conical section of the field of view of the optical probe extends to the cathode section before the inner wall of the heater truncates the field of view. Therefore, the view factors for these regions are constant in both cases and a ratio of 8.3 (6-inch nozzle to 13-inch nozzle) can be calculated for the view factor. The view factors for the regions upstream from the cathode, however, approach each other with both nozzles. At a location of 50 inches (1.27m) upstream of the nozzle throat, the ratio between both nozzles decreases to 2. Figure 20 illustrates the ratio between the two view factors in the IHF internal geometry. From the comparison of measured and simulated radiation heat fluxes at a distance of 10 inches to the 13-inch nozzle it can be concluded that more than 95% of the radiation heat

flux is generated in the discharge region (i.e. from the cathode position all the way upstream through the 15 feet (~4.6m) long arc-column). If, as a zeroth-order approximation, the thermochemical state inside the arc is considered to be constant (i.e., the same amount of radiation is emitted at each axial position), the incident radiation can be estimated by an integration over the view factors along the heater axis as plotted in Fig. 20.

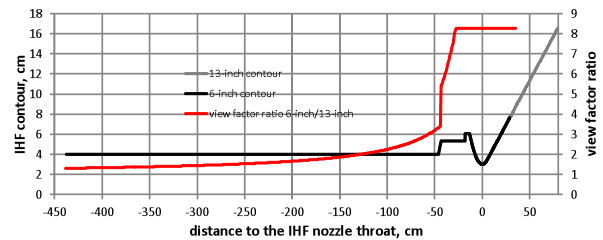


Figure 20. Ratio in view factors along the IHF axis between a test location of 10 inches distance to the 13-inch nozzle and 3 inches distance to the 6-inch nozzle for the same heater settings.

This very preliminary estimate of the contributions of the different arc-heater regions yields 30% radiation from the cathode region and 70% from the arc column for the 13-inch nozzle configuration. With the 6-inch nozzle, this ratio is approximately 50/50. These results yield an estimate of an increase in radiation heat flux by a factor of 3.3 by switching from a distance of 10 inches to the 13-inch nozzle exit to a location 3 inches from the 6-inch nozzle exit. However, absorption inside the plasma is not taken into account in these considerations. If the majority of radiation is generated in the cathode region (which would be the case if the arc-column is optically thick), the factor increases up to 8, which is considered an upper bound for the radiation increase between the two locations.

Comparing these estimates to the measured ratios at the MSL-8 condition (5.25 for bound-bound radiation, 2.45 for continuum), the majority of the measured bound-bound radiation must be generated in the cathode region of the arc heater. The measured continuum radiation, however, seems to be generated mainly close to the upstream electrode in the first part of the arc-column.

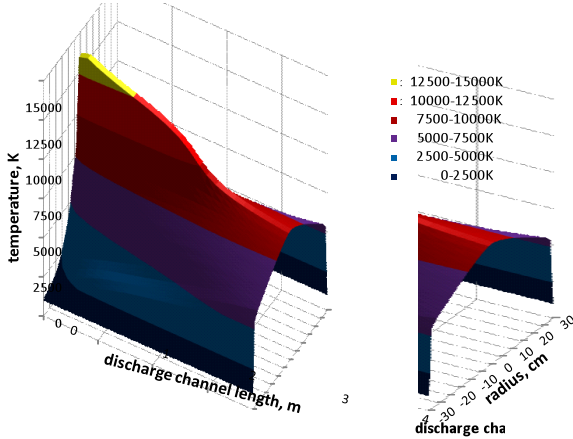


Figure 20. Temperature distribution in the IHF discharge channel at the MSL-8 condition computed with ARCFLO [17].

This result is in qualitative agreement with preliminary computations with the NASA code ARCFLO [17] of the plasma inside the arc-column showing a peak temperature decrease from about 15000K downstream of the anode to about 9000K in the cathode region, as shown in Fig. 20. Therefore, the arc-column seems to be at least partially optically thick for bound-bound radiation but not for continuum radiation.

Finally, radiation heat fluxes in the wavelength range from 250nm to 950nm were determined from the measured spectra by summing the emission spectra and multiplying with the corresponding wavelength increment for each pixel. Integrated over the spectral range from 250nm to 900nm, a value of 33 W/cm² is obtained for the high enthalpy condition MSL-8 which accounts for ~70% of the radiation heat flux measured in the radiometer set-up. Therefore, 30% of the radiative heat flux is produced in the UV between 160nm and 250nm and above 950nm, where the spectrometer set-up shows insufficient efficiency. From a theoretical simulation of the MSL-8 condition [3], about 44% of the total radiation was expected to be generated in the wavelength regions covered by the spectrometer data. The vacuum UV region below 160nm, which was not covered in the measurements, did contribute only with 1.2% of the total simulated radiation. The larger contribution of UV-NIR radiation as seen in the measurements may be attributed to the continuum radiation. However, the simulation regime was restricted to the region between plenum and probe and therefore did not include the discharge region

which contributes more than 95% to the total radiative heat flux. The next step will be to use the preliminary computations of the temperature in the discharge region to compute the chemical composition based on equilibrium assumptions. These values may then be used as input to *NEQAIR* to generate simulated spectra along lines of sight all the way to the probe position to simulate the spectral radiative heat fluxes.

The measured radiation heat fluxes scale almost linearly with the applied electrical power and with the calorimeter heat flux but not with the measured bulk enthalpy and account for up to 1.5% of the total heat flux to a 4-inch hemispherical calorimeter or 2.7% to a flat face. This may be considered negligible with respect to current uncertainties in measured heat flux. However, the measured spectra present an excellent opportunity to characterize the plasma inside the arc-heater.

5. SUMMARY AND CONCLUSIONS

A series of plasma diagnostics campaigns in the NASA Ames IHF arc-jet facility was conducted to characterize the conditions in different sections of the facility.

In the plenum of the arc-heater, comparison with CFD results showed a more varied radial emission profile in the experiment for the case of minimum added room temperature air and maximum bulk enthalpy of 21.6 MJ/kg. At the case with high add-air and low bulk enthalpy, the experimental results show a significantly higher plasma temperature. A preliminary estimate shows that the CFD temperature needs to be higher by about 1500K to match the measured spectra. Currently, a system to deduce enthalpy profiles from these measurements is in development.

The free stream measurements showed much stronger molecule emission from N₂ and NO than predicted based on the CFD computation. For the N₂ 1st Pos. system it was shown that inverse pre-dissociation gives a good explanation for the over population of high vibrationally excited levels. Applying a literature value for this process shows that the resulting N atom concentration determined from the molecule radiation is well within the theoretical limits for this plasma condition and surprisingly close to the CFD solution. For future analysis, ab-initio rate coefficients for inverse pre-dissociation and inclusion of more detailed modelling of population processes is anticipated to yield more reliable results for the atom densities, and therefore for the chemical contribution to local specific enthalpy.

The measured incident radiation on a probe surface at the material sample position shows that radiative heating from the inside of the arc-heater accounts for less than 3% of the total heat flux to a flat surface. The spectra showed strong continuum components which

are attributed to bound-free continua generated in the discharge channel. A spectral simulation of these signals based on an ARCFLOW solution is currently a work in progress.

6. ACKNOWLEDGMENTS

The present work was supported by NASA Contracts NAS2-03/44 to UARC, UC Santa Cruz, NNA04-BC25C to ELORET Corporation, NNA10DE12C to ERC Inc., and by the NASA-SCAP (Strategic Capabilities Assets Program) which provided critical financial support of the arc jet operational capability at Ames. The authors would like to thank Dr. George Raiche (Chief, Thermophysics Facilities Branch, NASA ARC) for generously providing test time in the IHF facility for the experiment, and the entire TSA branch for support of modeling and simulation aspects of the present work. Furthermore, the authors wish to acknowledge the support of Aga Goodsell, David Hash, Jay Grinstead, Jerry Ridge, Michael Olsen, Mark McGlaughlin, Brett Cruden, John Balboni, Joe Hartman, Anuscheh Nawaz, Eric Noyes, Lewis Ford, Jeffrey Mach, Roy Arakaki, Vince Meglio, Imelda Terrazas-Salinas, Enrique Carballo, and thank the arc jet crew for their professional and tireless effort to maintain and operate the arc jets under demanding schedule pressures.

7. REFERENCES

1. Winter, M W, Prabhu, D K, Taunk, J S, and Terrazas-Salinas, I, Emission Spectroscopic Measurements in the Plenum of the NASA IHF Arc Jet Facility, AIAA-2010-4522, 10th AIAA/ASME Joint Thermophysics and Heat Transfer Conference, Chicago, IL, 28 Jun - 1 Jul 2010.
2. Winter, M W, and Prabhu, D K, Excited State Chemistry in the Free Stream of the NASA IHF Arc Jet Facility Observed by Emission Spectroscopy, AIAA-2011-3632, 42nd AIAA Thermophysics Conference in Honolulu, Hawaii, 27 - 30 Jun 2011.
3. Winter, M.W., Prabhu, D.K., Raiche, G.A., Terrazas-Salinas, I., and Hui, F.C.L.. Emission Spectroscopic Measurements with an Optical Probe in the NASA Ames IHF Arc Jet Facility, AIAA-2012-1016, 50th AIAA Aerospace Sciences Meeting, Nashville, Tennessee, Jan. 9-12, 2012.
4. Winter, M.W., Raiche, G.A., Terrazas-Salinas, I., Hui, F.C.L., White, B., and Taunk, J.S., Measurements of Radiation Heat Flux to a Probe Surface in the NASA Ames IHF Arc Jet Facility, AIAA-2012-3189, 43rd AIAA Thermophysics Conference in New Orleans, Louisiana, June 25-28, 2012.
5. Prabhu, D K, et al., "CFD Analysis Framework for Arc-Heated Flowfields, I: Stagnation Testing in Arc-jets at NASA ARC," AIAA Paper AIAA-2009-4080, 41st Thermophysics Conference, June 22-25, 2009, San Antonio, TX.
7. Wright, M J, Candler, G V, and Bose, D, "Data-Parallel Line Relaxation Method of the Navier-Stokes Equations," AIAA Journal, Vol. 36, No. 9, 1998, pp. 1603-1609.
9. Whiting, E E, Park, C, Liu, Y, Arnold, J O, and Paterson, J A, "NEQAIR96, Nonequilibrium and Equilibrium Radiative Transport and Spectra Program: User's Manual," NASA RP-1389, NASA, December 1996.
11. Seong-Yoon Hyun, Chul Park, and Keun-Shik Chang, "Rate Parameters for Electronic Excitation of Diatomic Molecules, 4. NO Radiation," AIAA 2009-1595, 47th AIAA Aerospace Sciences Meeting, 5 - 8 January 2009, Orlando, Florida.
13. Babikian, D. S., Gopaul, N. K. J. L., and Park, C., "Measurement and Analysis of Nitric Oxide Radiation in an Arcjet flow," *Journal of Thermophysics and Heat Transfer*, Vol. 8, No. 4, October-December 1994, pp. 737-743.
15. Golde, M. F., and Thrush, B. A., "Afterglows," *Rep. Prog. Phys.* 1973, volume 36, pp 1285-1364, 1973.
11. Becker, K. H., Fink, E. H., Groth, W., Jud, W., and Kley, D., "N₂ formation in the Lewis-Rayleigh afterglow," *Faraday Discussions of the Chemical Society*, volume 53, pp35-51, 1972.
18. Partridge, H., Langhoff, S.R., Bauschlicher, C.W, and Schwenke, D.W., "Theoretical study of the A²Σ_g⁺ and C²Π_u states of N₂: Implications for the N₂ afterglow," *J. Chem. Phys.* 88 (5), 1 March 1988.
13. S. W. Benson, "Kinetic and Spectroscopic Constraints on the Origin of the N₂ Afterglow," *J. Chem. Phys.* 48,1765 (1968).
15. C.O. Laux et al., "State-to-state modeling of a recombining nitrogen plasma experiment", *Chem. Phys.* (2011).
17. A. Y. M. Ung, J., "Observations of the high vibrational levels of N₂(B³Π_g) in the Lewis-Rayleigh afterglow of nitrogen," *Chem. Phys.* 65, 2987 (1976).
17. Watson, V. R. and Pegot, E. B., "Numerical Calculations for the Characteristics of a Gas Flowing Axially Through a Constricted Arc," NASA TN D-4042, 1967.